

Wave-based extreme deep learning based on non-linear time-Floquet entanglement

Ali Momeni¹ and Romain Fleury^{1,*}

¹Laboratory of Wave Engineering, School of Electrical Engineering, Swiss Federal Institute of Technology in Lausanne (EPFL), Lausanne, Switzerland

*E-mail: romain.fleury@epfl.ch

ABSTRACT

Wave-based analog signal processing holds the promise of extremely fast, on-the-fly, power-efficient data processing, occurring as a wave propagates through an artificially engineered medium. Yet, due to the fundamentally weak non-linearities of traditional wave materials, such analog processors have been so far largely confined to simple linear projections such as image edge detection or matrix multiplications. Complex neuromorphic computing tasks, which inherently require strong non-linearities, have so far remained out-of-reach of wave-based solutions, with a few attempts that implemented non-linearities on the digital front, or used weak and inflexible non-linear sensors, restraining the learning performance. Here, we tackle this issue by demonstrating the relevance of Time-Floquet physics to induce a strong non-linear entanglement between signal inputs at different frequencies, enabling a power-efficient and versatile wave platform for analog extreme deep learning involving a single, uniformly modulated dielectric layer and a scattering medium. We prove the efficiency of the method for extreme learning machines and reservoir computing to solve a range of challenging learning tasks, from forecasting chaotic time series to the simultaneous classification of distinct datasets. Our results open the way for wave-based machine learning with high energy efficiency, speed and scalability.

1 Introduction

Recently, artificial intelligence (AI) systems based on advanced machine learning algorithms have attracted a surge of interest for their potential applications in processing the information hidden in large datasets^{1,2}. Wave-based analog implementations of these schemes, exploiting microwave or optical neural networks,

promise to revolutionize our ability to perform a large variety of challenging data processing tasks by allowing for power-efficient and fast neuromorphic computing at the speed of light. Indeed, wave-based analog processors work directly in the native domain of an analog signal, processing it while the wave propagates through an engineered artificial structure (metamaterials and metasurfaces)^{3–12}, as previously established in the cases of simple linear operations such as image differentiation, signal integration and integro-differential equations solving^{13–23}. For more complex processing tasks, for example image recognition or speech processing, both non-linearity and a high degree of interconnection between the elements are desired, requirements that have led to various proposals of neuromorphic processors exploiting optical diffraction, coupled waveguide networks, or disordered structures^{24–33}. A particularly vexing challenge, however, is the implementation of non-linear processing elements. While power-efficient neuromorphic schemes require a pronounced, particular form of non-linearities, optical non-linearities, such as in Kerr dielectrics, are typically weak at low intensities, and cannot be much controlled. This leads to sub-optimal systems that must operate with high input powers^{31,34,35}. As an alternative, non-linearities that are external to the wave-based processor have also been considered, for example by exploiting the intensity dependency of a sensor, that needs an additional electronic interconnection. Unfortunately, exploiting such weak and non-controllable non-linearities drastically confine the performance of most machine learning schemes, and the relevance of wave-based platforms have so far been largely restricted to the implementation of simple linear matrix projections.

Here, we propose to leverage the physics of wave systems that are periodically modulated in time, the so-called time-Floquet systems^{36–41}, to solve this vexing challenge by implementing a strong, controllable non-linear entanglement between all the input signals. We propose to use a simple, thin, uniform dielectric slab, whose refractive index is slowly and weakly modulated in time. With the addition of linear random scattering disorder, we implement very efficient recurrent neural networks (RNNs) schemes, namely extreme learning machine (ELM) and reservoir computing (RC). We demonstrate the high accuracy of our Floquet extreme learning machine in challenging computing tasks, from the processing of one-dimensional data (learning non-linear functions), to challenging multi-dimensional data (e.g. the abalone dataset classification problem). We also demonstrate the flexibility of our scheme that can be multiplexed to tackle two unrelated classification tasks at the same time, simultaneously sorting COVID-19 Xray lung

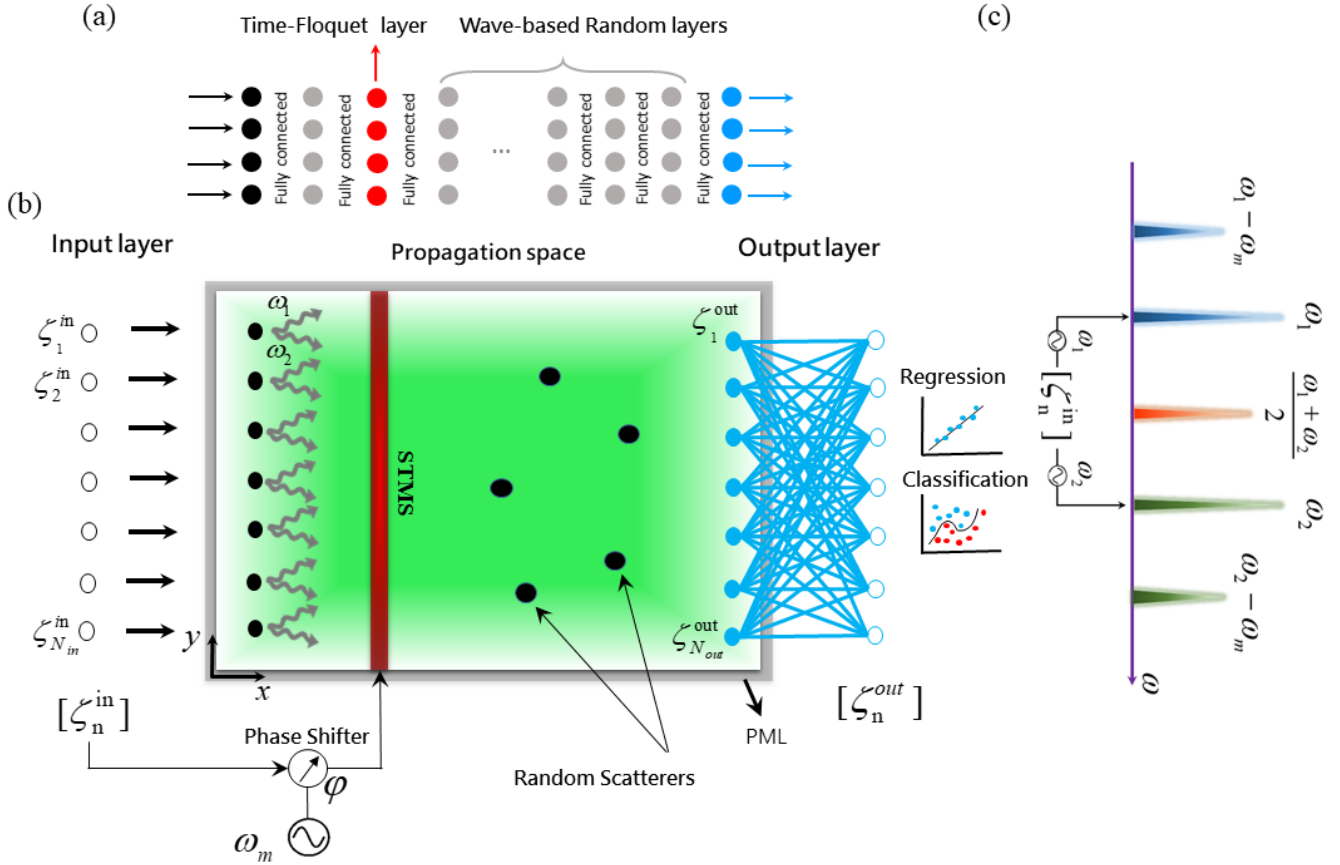


Figure 1. Wave based time-Floquet extreme learning machine. (a) Schematic of a neural network including a time-Floquet layer made from neurons whose properties are modulated periodically in time, and traditional random layers. Only the last layer (output) is trainable. (b) Concrete implementation with electromagnetic waves. The input signals ζ_n^{in} are modulated at ω_1 and ω_2 . Their sum forms input signals that are independently radiated into the surrounding space by an array of source antennas (black disks). As the waves propagate in the green region, they encounter a thin dielectric slab whose index of refraction is modulated at the frequency $\omega_m = |\omega_1 - \omega_2|/2$, as well as five sub-wavelength scatterers, randomly located in the domain. The modulation phase is assumed to depend on the input vector $\zeta_n^{\text{in}}(t)$. The gray rectangle represents an absorbing boundary layer. The output $\zeta_n^{\text{out}}(t)$ are fed into an adaptable blue dense layer, and used for regression and classification. (c) Non-linear phase entanglement. The modulated slab mixes signals at ω_1 and ω_2 into Floquet Harmonics spaced by ω_m , whose amplitudes depend non-linearly on the input vector.

images and hand-written digits. Finally, we validate our Floquet RC by predicting the time-evolution of a chaotic system over a large time-period (the Mackey-Glass time series). Such extreme time-Floquet analog learning machines are not only fast, easy-to-train, power efficient, and versatile, but also feature a unique accuracy performance that is comparable to that obtained with the best digital schemes.

2 Nonlinear time-Floquet-based extreme learning machine

We consider a particular class of neural networks, known as recurrent neural networks (RNNs). RNNs are ideal to process intricate data due to the internal cyclic connections between internal neurons, whose outputs depend on both the current inputs and the previous states of the neurons⁴². This memory effect allows RNNs to detect recursive relations in the data, which is relevant for example to process temporal signals. In digital implementations, however, the heavy internal connectivity matrices that are involved in the training process make RNNs particularly computationally-expensive and complicated^{43–46}. In order to solve these challenges, a number of alternative computing approaches such as long short-term memory (LSTM)⁴⁷, echo state networks (ESNs)⁴⁸, extreme learning machines (ELMs)^{49–51}, and reservoir computing (RC)^{44–46,52} have emerged. These schemes are particularly well suited for wave-based implementations, because waves propagation inherently relies on the inertial memory of the medium, which can be enhanced and engineered by leveraging resonant cavities, or multiple scattering. In addition, wave interferences are a particularly efficient way to create a high degree of interconnections between a large set of inputs.

Our time-Floquet neuromorphic processor implements an ELM, schematically shown in Fig. 1(a). ELMs, or closely related methods based on random neural networks⁵³ or support vector machines⁵⁴, are a powerful scheme in which only a last layer of connections is trained (in blue). The fundamental mechanism is the use of the non-trained part of the network, whose layers are represented in grey and red in Fig. 1(a), to establish a nonlinear mapping between the initial space of the dataset, and a higher-dimensional feature space, where a properly trained classifier performs the separation and classification. In our case, this non-linear mapping is performed by letting one of the non-trained layers (in red) be weakly modulated in time at a frequency much lower than the one of the signal, but with a phase that depends on the input state.

A concrete implementation of this scheme in a wave platform is shown in Fig. 1(b). It consists of three parts: (i), an array of monopole antennas that radiates the various components of the input vector into the surrounding medium; (ii), a propagation space composed of a few scatterers and a thin dielectric slab, called a scattering time-modulated slab (STMS), whose index of refraction is weakly modulated in time; and (iii), the output layer made of an array of receiving antennas and a single dense layer, digitally

trained to perform the desired regression or classification tasks. At the input layer, the input vector ζ^{in} with components $\zeta_1^{\text{in}}, \dots, \zeta_N^{\text{in}}$ is first encoded into N signals s_i^{in} , injected directly into the source antenna array. We assume that ζ^{in} is modulated at two distinct close-by frequencies ω_1 and ω_2 , such that:

$$s_i^{\text{in}} = \zeta_i^{\text{in}} \left(\sin(\omega_1 t) + \sin(\omega_2 t) \right). \quad (1)$$

The permittivity ϵ_r of the STMS is modulated with a depth δ_m and a phase ϕ , at a frequency $\omega_m = |\omega_1 - \omega_2|/2$, so that $\epsilon_r = \epsilon_s + \delta_m \cos(\omega_m t + \phi)$. This choice of modulation frequency allows for the two input frequency to be efficiently mixed at the dominant Floquet harmonic $(\omega_1 + \omega_2)/2$ (see Fig. 1(c)). As we will now see, the reflection and transmission coefficients of Floquet Harmonics show a strongly non-linear dependency on the modulation phase, a key property that we will leverage to make the ELM very efficient.

To understand how time-Floquet systems can be used to induce large non-linear entanglement between the incident and reflected signals, let us consider the toy model of a generic two-port time-Floquet system, where incident and reflected signals at ports 1 and 2 are represented by their time-varying complex amplitudes $a_{1,2}(t)$ and $b_{1,2}(t)$. This model applies for each plane wave incident on our STMS, with transverse wave number k , on which the actual field can be decomposed. Assuming the modulation frequency ω_m to be much smaller than the operation frequency ω_k ^{55,56}, we can neglect dispersive effects and write the following instantaneous relation between the signals at each ports:⁵⁵⁻⁵⁷

$$\begin{bmatrix} a_1(t) \\ b_1(t) \end{bmatrix} = \tilde{\Psi}(\omega_k, t) \begin{bmatrix} a_2(t) \\ b_2(t) \end{bmatrix}, \quad (2)$$

where $\tilde{\Psi}(\omega_k, t)$ is the transfer matrix at ω_k , which varies slowly with time. Taking the Fourier transform of both sides yields

$$\begin{bmatrix} A_1(\omega) \\ B_1(\omega) \end{bmatrix} = \tilde{\Psi}(\omega_k, \omega) * \begin{bmatrix} A_2(\omega) \\ B_2(\omega) \end{bmatrix} = \int \tilde{\Psi}(\omega_k, \omega - \omega') \begin{bmatrix} A_2(\omega') \\ B_2(\omega') \end{bmatrix} d\omega', \quad (3)$$

Since the scattering process into each Floquet harmonic component is linear, we can define the reflection

and transmission coefficients into each harmonic as $R_0(\omega_k + n\omega_m) = B_1(\omega_k + n\omega_m)/A_1(\omega_k)$ and $T_0(\omega_k + n\omega_m) = A_2(\omega_k + n\omega_m)/A_1(\omega_k)$. A direct calculation shows that (see Supplementary for detail derivations):

$$R_\phi(\omega_k + n\omega_m) = e^{in\phi} R_0(\omega_k + n\omega_m) \quad (4)$$

$$T_\phi(\omega_k + n\omega_m) = e^{in\phi} T_0(\omega_k + n\omega_m), \quad (5)$$

where we have used the notation R_ϕ to highlight the dependency of the scattering coefficients on the modulation phase ϕ . These equations imply that upon adding a phase delay ϕ to the modulation, the generated frequency harmonic of order n will acquire a phase shift of $n\phi$, both for the forward and backward scattered plane waves. On the other hand, the amplitude of harmonic waves are constant when we alter the phase delay.

Now, consider the superposition of two incident plane waves at frequencies ω_1 and ω_2 . Recalling our choice of modulation frequency, namely $\omega_m = |\omega_1 - \omega_2|/2$, we can write the reflection and transmission waves for all Floquet harmonic components of frequency $\omega_1 + n\omega_m = \omega_2 + m\omega_m$ by using the superposition principle:

$$|R'_\phi| = |e^{in\phi} R_0(\omega_1, \omega_1 + n\omega_m) + e^{im\phi} R_0(\omega_2, \omega_2 + m\omega_m)| \quad (6)$$

$$|T'_\phi| = |e^{in\phi} T_0(\omega_1, \omega_1 + n\omega_m) + e^{im\phi} T_0(\omega_2, \omega_2 + m\omega_m)|, \quad (7)$$

where n and m are the orders of the Floquet harmonics with respect to ω_1 and ω_2 , respectively. A particular example is the harmonic located at the average frequency $\omega = (\omega_1 + \omega_2)/2$, for which $n = 1 = -m$ (orange spectrum in Fig. 1(c)). According to Eqs. (6) and (7), the relation between the modulation phase and the intensity of scattered harmonic fields is highly nonlinear. In fact, we can control the amplitude of the Floquet harmonics only by changing the modulation phase. In order to have a nonlinear input-output mapping, we must therefore entangle the phase delay with the input input vector (i.e., $\phi = f(\zeta^{\text{in}})$), using for example a simple external signal mixer. In other words, the value of the modulation phase is directly determined by the value of the input vector, which is fixed when the system is excited, automatically making the scattering process a highly non-linear function of the input, regardless of the input power.

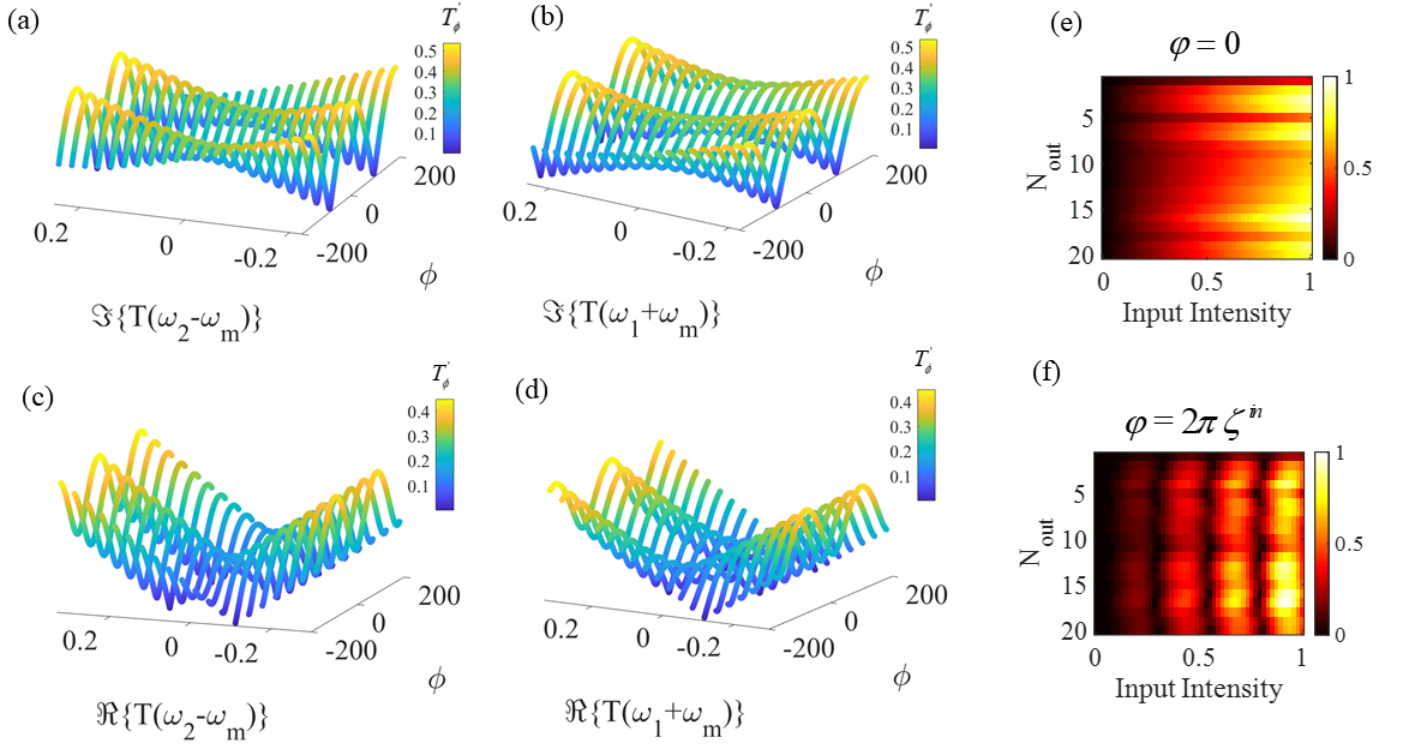


Figure 2. Non-linear Floquet entanglement (a)-(d) Theoretical demonstration of the nonlinear dependency of the intensity T'_ϕ of the central Floquet harmonic ($\omega = (\omega_1 + \omega_2)/2$) on both the modulation phase ϕ and the real or imaginary part of one of the generated harmonics. The results are based on Eq. (7). The fixed parameters for (a)-(d) are: (a): $T(\omega_1 + \omega_m) = 0.1 - 0.25i$ and $\Re\{T(\omega_2 - \omega_m)\} = 0.1$. (b): $T(\omega_2 - \omega_m) = 0.1 - 0.25i$ and $\Re\{T(\omega_1 + \omega_m)\} = 0.1$. (c): $T(\omega_1 + \omega_m) = 0.1 - 0.05i$ and $\Im\{T(\omega_2 - \omega_m)\} = 0.05$. (d): $T(\omega_2 - \omega_m) = 0.1 - 0.05i$ and $\Im\{T(\omega_1 + \omega_m)\} = 0.05$. (e) and (f) The numerical demonstration of linear/nonlinear Floquet entanglement for the central harmonic wave for different readout nodes in terms of input intensity, for static (e) and dynamic phase delays (f).

This makes such time-Floquet non-linear entanglement highly advantageous in neuromorphic computing schemes.

To exemplify the strong nonlinear response of the proposed system, we plot the amplitude of the transmitted central harmonic ($\omega = (\omega_1 + \omega_2)/2$) as a function of various variables, including the phase delay ϕ . The results are displayed in Figs. 2(a)-(d). We fix one of the harmonics and plot T'_ϕ versus the modulation phase and the real or imaginary part of the other transmitted harmonics, $T(\omega_1 + \omega_m)$ (or $T(\omega_2 - \omega_m)$). As we can see in Figs. 2(a)-(d), we indeed obtain a complex non-linear semi-sinusoidal form for T'_ϕ , upon altering the modulation phase. The dependency on the real or imaginary parts of the other transmitted harmonic is also always non-linear.

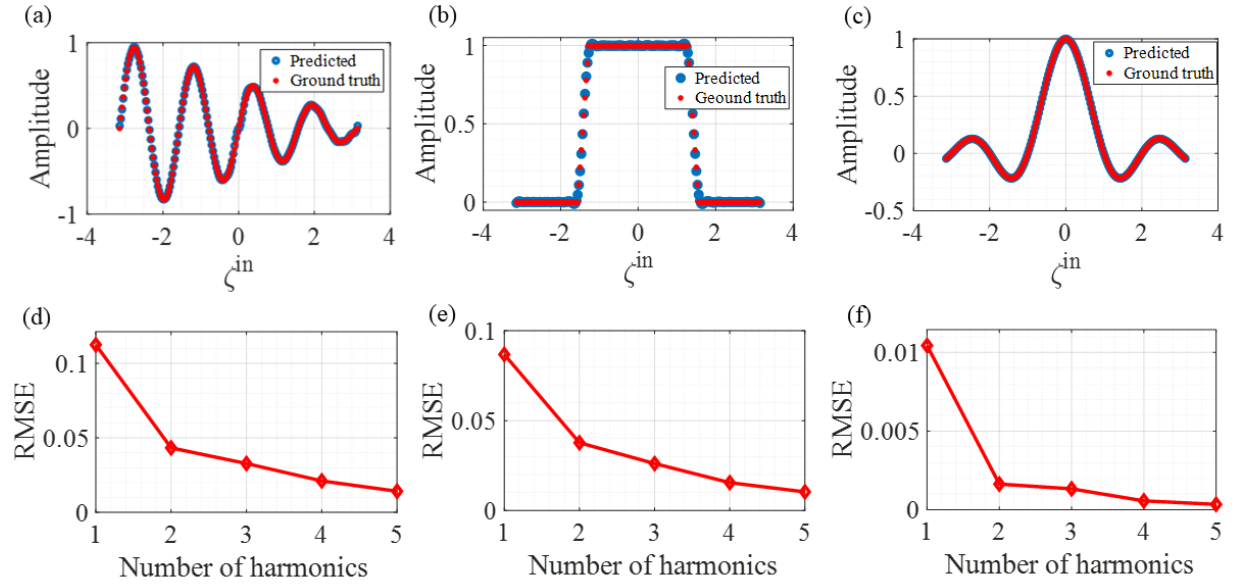


Figure 3. Floquet extreme learning for highly nonlinear maps: (a), (b), and (c) Comparison between ground truth and predicted values for three different nonlinear functions: $y_1 = \alpha \sin(4\pi\zeta^{\text{in}})(|\zeta^{\text{in}}|/\pi)$, and $y_2 = \text{rect}(\zeta^{\text{in}})$ and $y_3 = \sin(\pi\zeta^{\text{in}})/(\pi\zeta^{\text{in}})$, respectively. (d), (e), and (f) The corresponding values of root-mean-square error (RMSE) upon increasing the numbers of involved Floquet harmonics at the readout nodes.

Next, we implement the entanglement with the input vector to demonstrate the complex nonlinear behavior of the Floquet system, using a full-wave finite-difference time-domain simulation of the set-up of Fig. 1(b) (see Methods). We compute the intensity of the central harmonic with respect to the input intensity for two different scenarios: a static phase delay and a dynamic phase delay. In the first scenario, the phase delay is fixed and not dependent on the input ($\phi = 0$), and as shown in Fig. 2(e), the harmonic intensities are linear in term of input intensities. In the second scenario, the delay phase is a simple linear function of the input (i.e., $\phi = 2\pi\zeta^{\text{in}}$). Fig. 2(f) shows the complex nonlinear form of proposed system. The oscillating nonlinear mapping performed by the proposed system is completely different from any earlier approaches. As we will show, it is surprisingly effective in transforming the input data space to a nearly linearly separable output data space.

2.1 Learning highly nonlinear functions

We now demonstrate the performance of the Floquet ELM by starting with simple regression problems, on a dataset generated with nonlinear relations. Such dataset is often used as a standard benchmark in machine learning since linear regression of a nonlinear function is impossible without a nonlinear

transformation^{35,49}. The input information (ζ^{in}) is a set of randomly generated numbers between $-\pi$ to π and the corresponding output labels (y_i) are generated according to non-linear functions, namely $y_1 = \alpha \sin(4\pi\zeta^{\text{in}})(|\zeta^{\text{in}}|/\pi)$, $y_2 = \text{rect}(\zeta^{\text{in}})$ (pulse function), and $y_3 = \sin(\pi\zeta^{\text{in}})/(\pi\zeta^{\text{in}})$. We use 1000 randomly generated samples, which lie in $[-\pi, \pi]$ to cover the entire characteristic behavior of the function. We map each input value to a vector by multiplying it with a fixed random 1D vector (mask), here of dimension 1×10 . In this task, we use 10 input nodes and readout nodes. By recording the intensity of the harmonics in the readout nodes of many input values, a linear regression method is performed on the output data (see Figs. 3(a)-(c)). A remarkable learning performance, with very low root-mean-squared error (RMSE) for all three nonlinear functions, is obtained. Interestingly, in the proposed wave-based neural network with a nonlinear time-Floquet layer, the multiple generated harmonic fields can be used to extend the dimension of the nonlinear mapping, and increasing their number improves the accuracy of classification/regression. This tendency is demonstrated in Figs. 3(d)-(f), which plots the RMSE versus the number of considered Floquet harmonics. This mechanism is a clear advantage of the Floquet ELM: by involving a higher number of scattered harmonics, we can improve the RMSE and enhance the accuracy of learning with no additional computational cost. Note that, in the last layer, a fast Fourier transform (FFT) is performed on the time-series output data obtained from the readout nodes, in order to compute the intensity of the different harmonic waves (see further details in Methods). However, performing FFT requires only a simple multiplication and does not impose a large computational overhead.

2.2 Abalone dataset

In the previous section, we have used our Floquet ELM to learn nonlinear functions and its interpolation capability. However, interpolation is not always the relevant task, especially in complex inference problems. Therefore, we now move to a more challenging multivariable problem: the abalone dataset⁵⁸. This dataset is one of the most used benchmarks for machine learning, and concerns the classification of sea snails in terms of age and physical parameters. It lists eight physical features of sea snails that can be used for the prediction of their age. To tackle this problem with our Floquet ELM, we encode the 8 physical features of sea snails on our input nodes, and consider 50 readout nodes to feed the decision layer, which performs linear regression. Fig. 4(a) presents the true ages and the corresponding predictions; the figure indicates

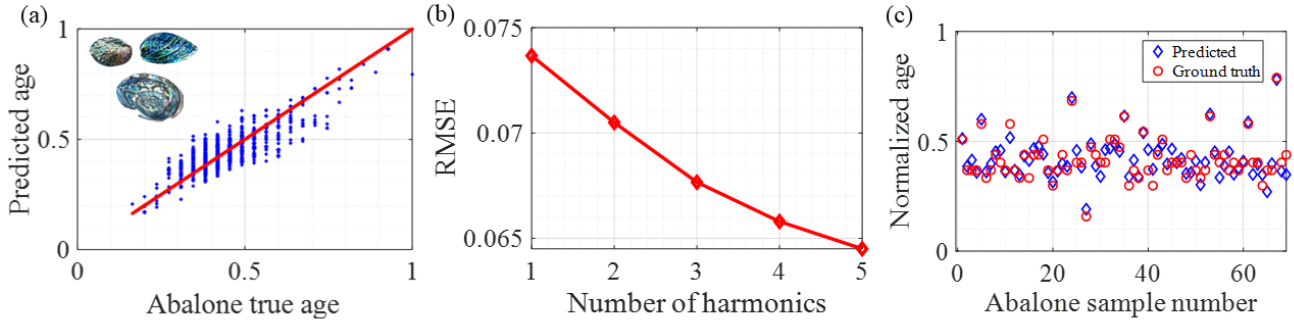


Figure 4. Floquet extreme learning for multi-variable regression: (a) and (b) Learning of the abalone dataset and corresponding RMSE for different numbers of considered harmonic waves, respectively. (c) Comparison between predicted data (blue) and ground truth (red).

that the framework learns the ages of the abalone with remarkable accuracy. For a direct comparison, we plot the predicted values for 75 random input data (Fig. 4(c)). The RMSE with respect to number of harmonic waves are plotted in Fig. 4(b). A remarkable accuracy (RMSE=0.064) can be achieved by considering five generated harmonics. The achieved RMSE, is smaller than state-of-the-art reported values³⁵.

2.3 Parallel image classifications

Another remarkable feature of time-Floquet systems is that since the inputs are modulated at a certain carrier frequency, we can use several frequency bands and multiplex different signals to classify them simultaneously using the same system, and no additional cost in terms of power consumption. Let us now demonstrate this in a specific complex parallel classification task. We examine the possibility to perform parallel image classification using two wavelength inputs. We use two distinct datasets: the MNIST dataset of handwritten digits⁵⁹ and the COVID-19 X-ray images⁶⁰ (see Figs. 5(a) and (b)). We resize all of images into 10×10 pixels, down-sampling them to decrease the number of input and readout nodes and the total size of our structure. In this task, we use 100 nodes to encode the images with the amplitude of the input waves. The MNIST data are encoded onto a (randomly selected) frequency range from 4 to 4.125 THz, and the COVID-19 data are encoded between 4.375 and 4.5 THz (see the red and blue frequency bands in Fig. 5(c)). In the output layer, we use Softmax regression to perform classifications (See Methods).

The training results are shown in Figs. 5(d)-(g). The observed test accuracies were 88.2% for the

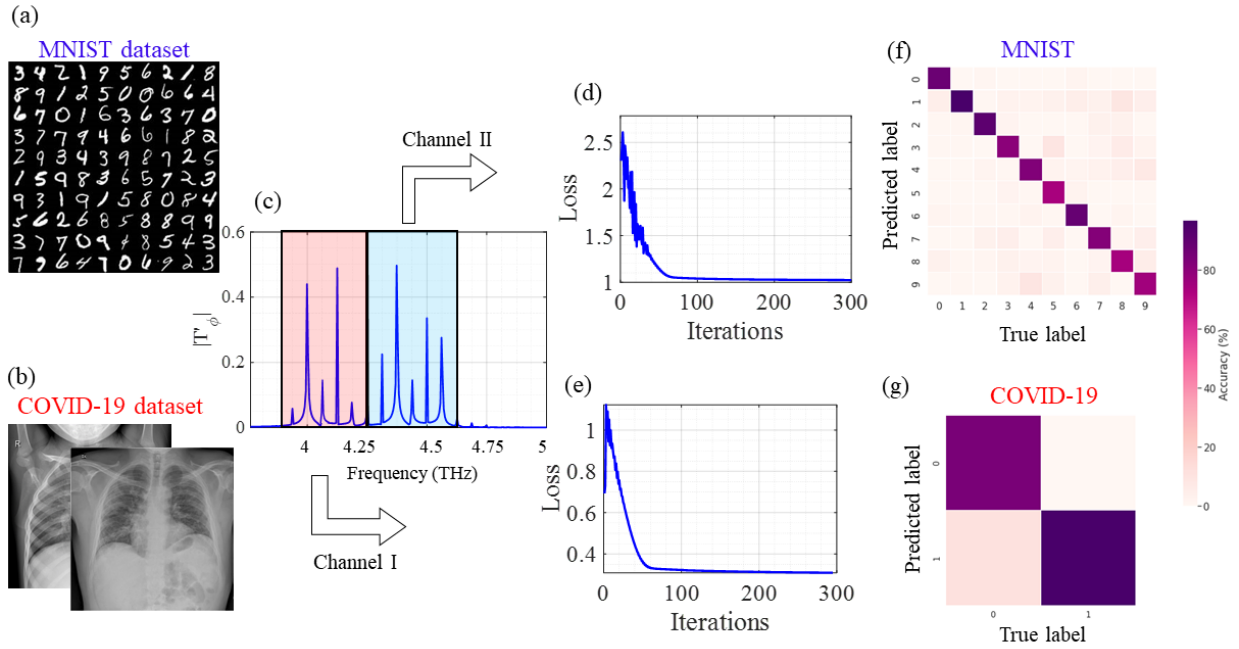


Figure 5. Floquet extreme learning for parallel image classification. (a) and (b) Examples of realizations taken from the MNIST and COVID-19 X-ray datasets. (c) Simulated spectra of readout nodes for two different channels. (d) and (e) Evolution of the loss function for MNIST and COVID-19 classifications, respectively. (f) and (g) Corresponding confusion matrices, for condition classification.

COVID-19 and 85.3% for the MNIST datasets. These classification accuracies are competitive. For example, they are higher than the ones reported in reference⁴³ (parallel image classification). Also, the classification-accuracy results are comparable with other relevant works despite the decreasing the pixel sizes of all images⁴⁶. In addition, this frequency multiplexing technique is the first demonstration of wave-based parallel task processing with extreme deep learning. This enables the use of wide-bandwidth as a computational resource, which significantly boosts the computation efficiency.

3 Nonlinear Time-Floquet-based RC system for autonomous forecasting chaotic time-series

To show the high versatility of the proposed nonlinear time-Floquet neuromorphic computing system, we slightly modify it to implement a reservoir computing (RC) scheme. Consider an input vector $i(t)$ that is injected to a high-dimensional dynamical system called the reservoir. The reservoir is described by a vector $h(t)$ and the initial state of the reservoir is defined randomly. Let the W_{res} matrix define

the internal connections of the reservoir nodes and the W_{in} matrix define the connections between the input and the reservoir nodes. Both matrices are initialized randomly and fixed during the whole RC training process. The state of each reservoir node is a scalar $h(t)$, which evolves according to the following recursive relation:

$$h(t + \tau) = F\left(w_{in}i(t) + w_{res}h(t)\right) \quad (8)$$

where τ is the discrete time step of the input and F is a nonlinear function. From Eq. (8), we see that the reservoir is defined as a dynamical system provided with a unique memory property; namely, each consequent state of the reservoir contains some information about its previous states and about the inputs injected until that time. In the training phase, the input $i(t)$ is fed to the reservoir, and the corresponding reservoir states are recursively calculated. The final step of the information processing is to perform a simple linear regression in order to minimize the RMSE that adjusts the W_{out} weights. The output can be computed with $O(t) = W_{out}h(t)$. It should be noted that the output weights are the only parameters that are modified during the training. The input and reservoir weights are fixed throughout the whole computational process, and they are used to randomly project the input into a highdimensional space, which increases the linear separability of inputs.

In our concrete scheme, we implement this memory using a feedback-loop, and use the intensity of harmonic waves as a reservoir states. The reservoir computing in our scheme can be described by the following recursive relation:

$$T'_{\phi}(t + \tau) = F\left(w_{in}i(t) + w_{res}v_h T'_{\phi}(t)\right) \quad (9)$$

where F the nonlinear function describing our system, v_h is a tunable parameter that selects one (or more) harmonics as reservoir states and T'_{ϕ} is the intensity of transmission harmonic waves. In general, the RC and its different implementations have proven to be very successful for various tasks, such as spoken digits recognition, temporal Exclusive OR task, Mackey-Glass, or Nonlinear Autoregressive Moving Average

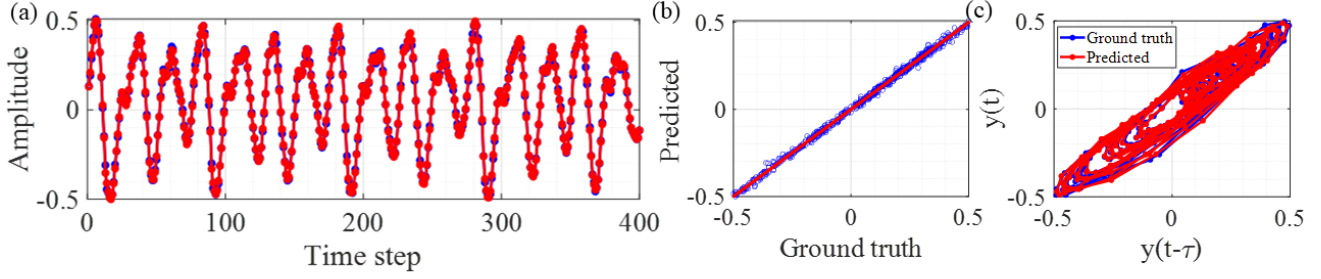


Figure 6. Floquet reservoir computing for forecasting the chaotic Mackey Glass time series. (a) Training results: The ground truth (blue) and the predicted output from the RC system (red) are plotted. (b) Corresponding results of linear regression. (c) Trace of time-series values in phase space, with respect to the previous time step for both ground truth and predicted values.

time-series prediction^{61,62}.

We use the nonlinear time-Floquet RC for prediction of chaotic time series. Forecasting chaotic time series is an extremely difficult task due to the accumulation of quantitative difference between the ground truth and the predicted value in subsequent predictions, that lead to exponential errors at large times. Indeed, the positive Lyapunov exponent in chaotic systems leads to exponential growth for the separation of close trajectories, so that even small errors in prediction can quickly lead to divergence of the prediction from the ground truth⁴². We test our system using the Mackey–Glass time series defined by^{42,63}.

$$\frac{dy}{dt} = \beta \frac{y(t-\tau)}{1 + (y(t-\tau))^n} - \gamma y(t) \quad (10)$$

Unlike for deterministic equation, predicting such time-series for specific values of parameters is difficult and thus have been widely used as a benchmark for challenging forecasting tasks. To obtain chaotic dynamics, here, we set the parameters $\beta = 0.2$, $\gamma = 0.1$, $\tau = 18$, $n = 10$. During the training phase, as soon as the reservoir states are calculated, a simple linear regression is executed to adjust the W_{out} weights such that their linear combination with the calculated reservoir states makes the actual output as close as possible to the next time step of the input. Finally, to automatically predict the future evolution of $i(t)$, we make a feedback-loop from the output to the input by replacing the next input $i(t+1)$ with the one-step prediction $W_{\text{out}}o(t)$, as is done in conventional RC. The ability of the proposed RC system in time-series prediction is tested using a reservoir with 75 nodes. We consider the middle harmonic as a reservoir state and input, ζ_n^{in} , to feed our RC system for each interactions (Eq. (9)). All of intensity harmonics, reservoir

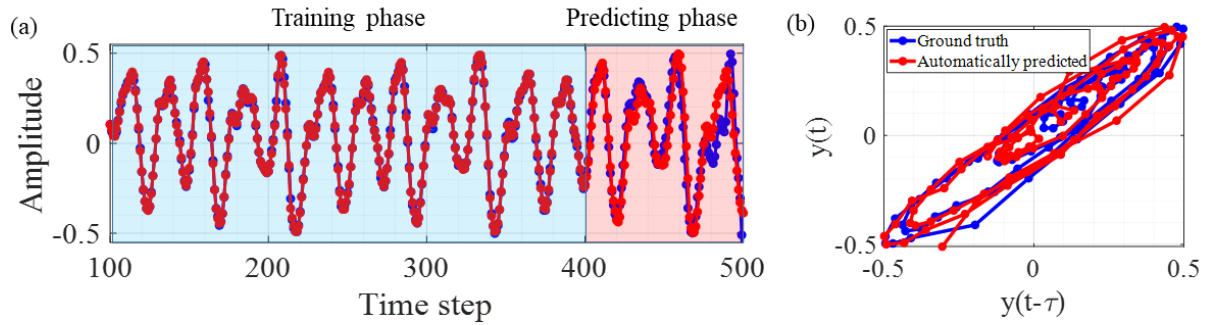


Figure 7. Autonomous forecasting of Mackey–Glass time series. Training and forecasting results: The ground truth (blue) and the predicted output from the RC system (red) for 100 next time steps are plotted. (c) Trace of time-series values, phase space, for predicting phase with respect to the previous time step.

states, are then applied to the readout layer (see Methods) to generate the predicted data for the next time step. Fig. 6 show the results obtained during training from the simulation. Excellent agreement between the target and the predicted value can be obtained, indicating that the trained readout weights can correctly calculate the next time-step signal on the basis of the internal states of the reservoir. Further evidence of successful training can be found by examining the network performance in regression and phase space, as shown in Figs. 6(b)-(c), where an excellent agreement can again be observed .

The network is then used to forecast the time series autonomously. After training for 400 time steps, the output from the readout function, that is, the predicted data for the next time step, is then connected to the reservoir as the new input, and the system autonomously produces the forecasted time series continuously. Fig. 7 show the results for autonomous time-series prediction using the proposed RC system. Afterwards, the autonomously generated output (from the 400th time step onwards) still matches very well the ground truth, showing the ability of the proposed RC system to autonomously forecast the chaotic system. After more than 70 time steps of autonomous prediction, the predicted signal starts to diverge from the correct value, which is unavoidable due to the chaotic nature of the series. Increasing the size of the reservoir further, by using more nodes and using more previous states may reduce the prediction error so that the length of accurate prediction can be increased. Another solution for long-term forecasting without increasing the dimension of the system is utilizing a periodical update procedure as in Ref.⁴².

4 Conclusion

In conclusion, we have shown how non-linear Floquet entanglement can be used to enable wave-based neuromorphic computing, by allowing for strong and tailored non-linear mapping to a higher dimensional space. Our nonlinear time-Floquet learning machine can process information to compute complex tasks that are traditionally only tackled by slower, sophisticated, digital deep neural networks. In our benchmarks, the proposed computing platform performs as well as its digital counterparts. With better energy efficiency in comparison to the previous proposals and a path to high scalability, our nonlinear time-Floquet system provides a novel path toward supercomputer-level optical computation.

5 Methods

5.1 Numerical simulations

We use a two-dimensional finite-difference time-domain (FDTD) method for all simulations^{64,65}. Fig. 8 shows the rectangular layout of the utilized setup. We set the parameters $\epsilon_{rs} = 3$, $\delta_m = 0.3$, $\omega_m = |\omega_1 - \omega_2|/2$, $Y = 8\lambda_0$, and $X = 15\lambda_0$. Also, the time window of simulation and the spatial window (time- and space-discretization factors) is set as a $d_t = d_{x,y}/(2C)$ and $d_{x,y} = \lambda_0/30$, respectively (C is speed of light). We use 10000 time-steps to ensure convergence has happened. In order to calculate the intensity of different harmonic waves, a simple fast Fourier transform (FFT) is performed.

5.2 Training of readout

For learning nonlinear functions, Abolone dataset, and forecasting chaotic time series, we used a supervised learning algorithm, linear regression, to train the readout function. The predicted output is compared with the ground truth, and the error is calculated and used to update the weights in the readout network following the linear regression learning rule.

To train the readout network, for classification task parallel image processing, we used the Python toolkit Keras, which provides a high-level application programming interface to access TensorFlow. A supervised learning algorithm, softmax regression, was used to train the readout network. A softmax function is used as the activation function of the readout network to calculate the probability corresponding to the different possible outputs. The cost is calculated following a categorical crossentropy. A standard

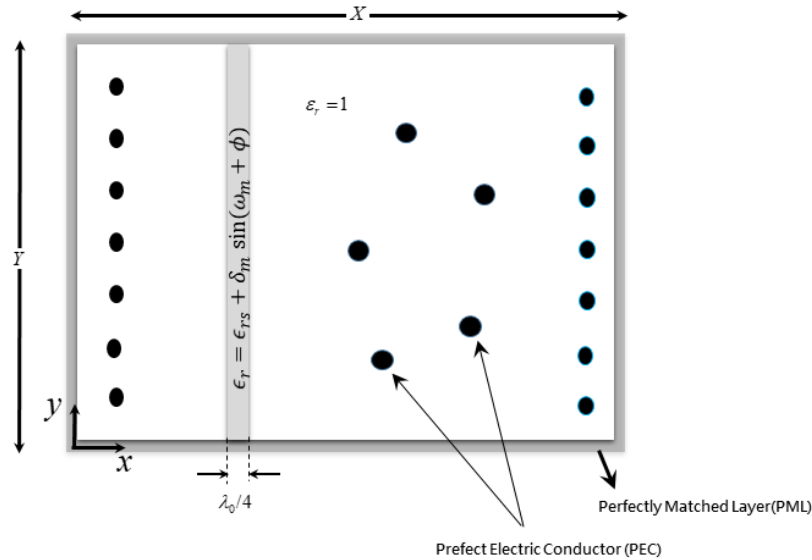


Figure 8. Layout of the setup. Black disks are an array of hard source (left side as an input array and right side as a receivers). The gray rectangle in the propagating substrate is a thin dielectric slab whose index of refraction is modulated at the frequency ω_m and five PEC sub-wavelength scatterers, randomly located in the propagating substrate. The gray rectangle represents an absorbing boundary layer.

gradient-based optimization method is used to minimize the cost function and train the output network. There are several ways of converting images into one-dimensional representations. For simplicity, we used a flattened version of downsampled images as an output vector.

Acknowledgements: A. Momeni and R. Fleury acknowledge funding from the Swiss National Science Foundation under the Eccellenza grant number 181232.

References

1. LeCun, Y., Bengio, Y. & Hinton, G. Deep learning. *nature* **521**, 436–444 (2015).
2. Shen, Y. *et al.* Deep learning with coherent nanophotonic circuits. *Nat. Photonics* **11**, 441 (2017).
3. Engheta, N. & Ziolkowski, R. W. *Metamaterials: physics and engineering explorations* (John Wiley & Sons, 2006).
4. Achouri, K. & Caloz, C. *Electromagnetic Metasurfaces: Theory and Applications* (John Wiley & Sons, 2021).

5. Li, L. *et al.* Machine-learning reprogrammable metasurface imager. *Nat. communications* **10**, 1–8 (2019).
6. Lin, D., Fan, P., Hasman, E. & Brongersma, M. L. Dielectric gradient metasurface optical elements. *science* **345**, 298–302 (2014).
7. Momeni, A., Rouhi, K., Rajabalipanah, H. & Abdolali, A. An information theory-inspired strategy for design of re-programmable encrypted graphene-based coding metasurfaces at terahertz frequencies. *Sci. reports* **8**, 1–13 (2018).
8. Kiani, M., Tayarani, M., Momeni, A., Rajabalipanah, H. & Abdolali, A. Self-biased tri-state power-multiplexed digital metasurface operating at microwave frequencies. *Opt. express* **28**, 5410–5422 (2020).
9. Kiani, M., Momeni, A., Tayarani, M. & Ding, C. Spatial wave control using a self-biased nonlinear metasurface at microwave frequencies. *Opt. express* **28**, 35128–35142 (2020).
10. Hosseinijad, S. E. *et al.* Digital metasurface based on graphene: An application to beam steering in terahertz plasmonic antennas. *IEEE Transactions on Nanotechnol.* **18**, 734–746 (2019).
11. Rajabalipanah, H., Abdolali, A., Shabanpour, J., Momeni, A. & Cheldavi, A. Asymmetric spatial power dividers using phase–amplitude metasurfaces driven by Huygens principle. *ACS omega* **4**, 14340–14352 (2019).
12. Hosseinijad, S. E. *et al.* Reprogrammable graphene-based metasurface mirror with adaptive focal point for THz imaging. *Sci. reports* **9**, 1–9 (2019).
13. Silva, A. *et al.* Performing mathematical operations with metamaterials. *Sci.* **343**, 160–163 (2014).
14. Camacho, M., Edwards, B. & Engheta, N. A single inverse-designed photonic structure that performs parallel computing. *Nat. Commun.* **12**, 1–7 (2021).
15. Estakhri, N. M., Edwards, B. & Engheta, N. Inverse-designed metastructures that solve equations. *Sci.* **363**, 1333–1338 (2019).
16. Zangeneh-Nejad, F., Sounas, D. L., Alù, A. & Fleury, R. Analogue computing with metamaterials. *Nat. Rev. Mater.* 1–19 (2020).

17. Zangeneh-Nejad, F. & Fleury, R. Topological analog signal processing. *Nat. communications* **10**, 1–10 (2019).
18. Momeni, A., Rajabalipanah, H., Abdolali, A. & Achouri, K. Generalized optical signal processing based on multioperator metasurfaces synthesized by susceptibility tensors. *Phys. Rev. Appl.* **11**, 064042 (2019).
19. Babae, A., Momeni, A., Abdolali, A. & Fleury, R. Parallel analog computing based on a 2×2 multiple-input multiple-output metasurface processor with asymmetric response. *Phys. Rev. Appl.* **15**, 044015 (2021).
20. Momeni, A., Rouhi, K. & Fleury, R. Switchable and simultaneous spatiotemporal analog computing. *arXiv preprint arXiv:2104.10801* (2021).
21. Momeni, A. *et al.* Reciprocal metasurfaces for on-axis reflective optical computing. *arXiv preprint arXiv:2012.12120* (2020).
22. Momeni, A., Safari, M., Abdolali, A., Kherani, N. P. & Fleury, R. Asymmetric metal-dielectric metacylinders and their potential applications from engineering scattering patterns to spatial optical signal processing. *Phys. Rev. Appl.* **15**, 034010 (2021).
23. Abdolali, A., Momeni, A., Rajabalipanah, H. & Achouri, K. Parallel integro-differential equation solving via multi-channel reciprocal bianisotropic metasurface augmented by normal susceptibilities. *New J. Phys.* **21**, 113048 (2019).
24. Wetzstein, G. *et al.* Inference in artificial intelligence with deep optics and photonics. *Nat.* **588**, 39–47 (2020).
25. Lin, X. *et al.* All-optical machine learning using diffractive deep neural networks. *Sci.* **361**, 1004–1008 (2018).
26. Zhang, H. *et al.* An optical neural chip for implementing complex-valued neural network. *Nat. Commun.* **12**, 1–11 (2021).
27. Zuo, Y. *et al.* All-optical neural network with nonlinear activation functions. *Opt.* **6**, 1132–1137 (2019).

28. Qian, C. *et al.* Performing optical logic operations by a diffractive neural network. *Light. Sci. & Appl.* **9**, 1–7 (2020).
29. Xu, X. *et al.* Photonic perceptron based on a kerr microcomb for high-speed, scalable, optical neural networks. *Laser & Photonics Rev.* **14**, 2000070 (2020).
30. Feldmann, J., Youngblood, N., Wright, C. D., Bhaskaran, H. & Pernice, W. H. All-optical spiking neurosynaptic networks with self-learning capabilities. *Nat.* **569**, 208–214 (2019).
31. Hughes, T. W., Williamson, I. A., Minkov, M. & Fan, S. Wave physics as an analog recurrent neural network. *Sci. advances* **5**, eaay6946 (2019).
32. Hamerly, R., Bernstein, L., Sludds, A., Soljačić, M. & Englund, D. Large-scale optical neural networks based on photoelectric multiplication. *Phys. Rev. X* **9**, 021032 (2019).
33. Bueno, J. *et al.* Reinforcement learning in a large-scale photonic recurrent neural network. *Opt.* **5**, 756–760 (2018).
34. Papp, A., Porod, W. & Csaba, G. Nanoscale neural network using non-linear spin-wave interference. *arXiv preprint arXiv:2012.04594* (2020).
35. Teğin, U., Yıldırım, M., Oğuz, İ., Moser, C. & Psaltis, D. Scalable optical learning operator. *arXiv preprint arXiv:2012.12404* (2020).
36. Fleury, R., Khanikaev, A. B. & Alu, A. Floquet topological insulators for sound. *Nat. communications* **7**, 1–11 (2016).
37. Wang, X. *et al.* Nonreciprocity in bianisotropic systems with uniform time modulation. *Phys. Rev. Lett.* **125**, 266102 (2020).
38. Koutserimpas, T. T. & Fleury, R. Nonreciprocal gain in non-hermitian time-floquet systems. *Phys. review letters* **120**, 087401 (2018).
39. Estep, N. A., Sounas, D. L., Soric, J. & Alù, A. Magnetic-free non-reciprocity and isolation based on parametrically modulated coupled-resonator loops. *Nat. Phys.* **10**, 923–927 (2014).
40. Hadad, Y., Sounas, D. L. & Alu, A. Space-time gradient metasurfaces. *Phys. Rev. B* **92**, 100304 (2015).

41. Koutserimpas, T. T., Alù, A. & Fleury, R. Parametric amplification and bidirectional invisibility in pt-symmetric time-floquet systems. *Phys. Rev. A* **97**, 013839 (2018).
42. Moon, J. *et al.* Temporal data classification and forecasting using a memristor-based reservoir computing system. *Nat. Electron.* **2**, 480–487 (2019).
43. Nakajima, M., Tanaka, K. & Hashimoto, T. Scalable reservoir computing on coherent linear photonic processor. *Commun. Phys.* **4**, 1–12 (2021).
44. Du, C. *et al.* Reservoir computing using dynamic memristors for temporal information processing. *Nat. communications* **8**, 1–10 (2017).
45. Zhong, Y. *et al.* Dynamic memristor-based reservoir computing for high-efficiency temporal signal processing. *Nat. Commun.* **12**, 1–9 (2021).
46. Midya, R. *et al.* Reservoir computing using diffusive memristors. *Adv. Intell. Syst.* **1**, 1900084 (2019).
47. Hochreiter, S. & Schmidhuber, J. Long short-term memory. *Neural computation* **9**, 1735–1780 (1997).
48. Dong, J., Gigan, S., Krzakala, F. & Wainrib, G. Scaling up echo-state networks with multiple light scattering. In *2018 IEEE Statistical Signal Processing Workshop (SSP)*, 448–452 (IEEE, 2018).
49. Huang, G.-B., Zhu, Q.-Y. & Siew, C.-K. Extreme learning machine: theory and applications. *Neurocomputing* **70**, 489–501 (2006).
50. Marcucci, G., Pierangeli, D. & Conti, C. Theory of neuromorphic computing by waves: machine learning by rogue waves, dispersive shocks, and solitons. *Phys. Rev. Lett.* **125**, 093901 (2020).
51. Pierangeli, D., Marcucci, G. & Conti, C. Photonic extreme learning machine by free-space optical propagation. *arXiv preprint arXiv:2105.12123* (2021).
52. Vandoorne, K. *et al.* Experimental demonstration of reservoir computing on a silicon photonics chip. *Nat. communications* **5**, 1–6 (2014).
53. Pao, Y.-H., Park, G.-H. & Sobajic, D. J. Learning and generalization characteristics of the random vector functional-link net. *Neurocomputing* **6**, 163–180 (1994).

54. Suykens, J. A. & Vandewalle, J. Least squares support vector machine classifiers. *Neural processing letters* **9**, 293–300 (1999).
55. Mousavi, S. H., Rakich, P. T. & Wang, Z. Strong thz and infrared optical forces on a suspended single-layer graphene sheet. *ACS photonics* **1**, 1107–1115 (2014).
56. Salary, M. M., Jafar-Zanjani, S. & Mosallaei, H. Electrically tunable harmonics in time-modulated metasurfaces for wavefront engineering. *New J. Phys.* **20**, 123023 (2018).
57. Salary, M. M., Jafar-Zanjani, S. & Mosallaei, H. Time-varying metamaterials based on graphene-wrapped microwires: Modeling and potential applications. *Phys. Rev. B* **97**, 115421 (2018).
58. Abalone datasets. <https://archive.ics.uci.edu/ml/datasets/Abalone>.
59. Mnist datasets. <https://www.tensorflow.org/datasets/catalog/mnist>.
60. Covid-19 datasets. <https://www.kaggle.com/tawsifurrahman/covid19-radiography-database>.
61. Brunner, D. *et al.* Tutorial: Photonic neural networks in delay systems. *J. applied physics* **124**, 152004 (2018).
62. Bertschinger, N. & Natschläger, T. Real-time computation at the edge of chaos in recurrent neural networks. *Neural computation* **16**, 1413–1436 (2004).
63. Mackey, M. C. & Glass, L. Oscillation and chaos in physiological control systems. *Sci.* **197**, 287–289 (1977).
64. Elsherbeni, A. Z. & Demir, V. *The finite-difference time-domain method for electromagnetics with MATLAB simulations* (The Institution of Engineering and Technology, 2016).
65. Kunz, K. S. & Luebbers, R. J. *The finite difference time domain method for electromagnetics* (CRC press, 1993).

6 SUPPLEMENTARY MATERIAL

The transfer matrix equation relating the amplitudes of the fields on opposite sides of the time-Floquet system (See Fig. 9) can be expressed in multiplicative form in time-domain for each excitation frequency as

$$\begin{bmatrix} a_1(t) \\ b_1(t) \end{bmatrix} = \tilde{\Psi}(\omega_k, t) \begin{bmatrix} a_2(t) \\ b_2(t) \end{bmatrix} \quad (11)$$

where $\tilde{\Psi}(\omega_k, t)$ is the time-varying transfer matrix. The transfer matrix equation can be taken into angular frequency domain by taking the Fourier transform of both sides as:

$$\begin{bmatrix} A_1(\omega) \\ B_1(\omega) \end{bmatrix} = \tilde{\Psi}(\omega_k, \omega) * \begin{bmatrix} A_2(\omega) \\ B_2(\omega) \end{bmatrix} = \int \tilde{\Psi}(\omega_k, \omega - \omega') \begin{bmatrix} A_2(\omega') \\ B_2(\omega') \end{bmatrix} d\omega' \quad (12)$$

Equation (12) implies that an input frequency ω_k will be converted to a spectrum of output frequencies. In the time-Floquet system, when the elements are varying in time with a periodic modulation having a modulation frequency of ω_m , $\varepsilon_r = \varepsilon_s + \delta_m \cos(\omega_m t)$, the transfer matrix is also periodic and can be expanded in form a Fourier series as $\tilde{\Psi}(t) = \sum_n \tilde{\Psi}^n(\omega_k) e^{in\omega_m t}$. And the Fourier transform takes the following form:

$$\tilde{\Psi}(\omega) = \sum_n \tilde{\Psi}^n(\omega_k) \delta(\omega - n\omega_m) \quad (13)$$

By choosing $\omega = \omega_q = \omega_k + q\omega_m$ and $\omega' = \omega_p = \omega_k + p\omega_m$, q and $p \in \{\dots, -1, 0, +1, \dots\}$, and substituting equations (13) into (12), we will arrive at the following equations⁵⁶:

$$\left\{ \begin{bmatrix} A_1(\omega_q) \\ B_1(\omega_q) \end{bmatrix} \right\} = \{ \tilde{\Psi}^{q-p}(\omega_k) \} \left\{ \begin{bmatrix} A_2(\omega_p) \\ B_2(\omega_p) \end{bmatrix} \right\} \quad (14)$$

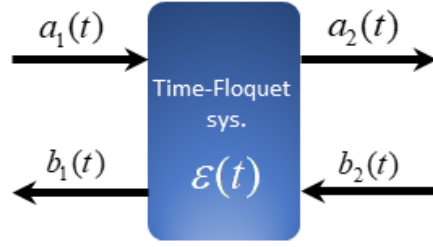


Figure 9. The schematic of a generic two-port time-Floquet system. Incident and reflected signals at ports 1 and 2 are represented by their time-varying complex amplitudes $a_{1,2}(t)$, and $b_{1,2}(t)$.

Now, let us consider adding a phase delay of ϕ to the sinusoidal modulation profile. Writing Equation (14) for the phase-delayed modulation and using $\tilde{\Psi}_\phi^{q-p}(\omega_k) = \exp(i(q-p)\phi)\tilde{\Psi}_\phi^{q-p}(\omega_k)$, we have:

$$\left\{ \begin{bmatrix} A_1^{(\phi)}(\omega_q) \\ B_1^{(\phi)}(\omega_q) \end{bmatrix} \right\} = \{e^{i(q-p)\phi}\tilde{\Psi}_\phi^{q-p}(\omega_k)\} \left\{ \begin{bmatrix} A_2^{(\phi)}(\omega_p) \\ 0 \end{bmatrix} \right\} \quad (15)$$

By setting $B_2(\omega_p) = 0$ for all p 's and $A_1(\omega_q) = 0$ for all q 's except $A_1(\omega_0) = 1$, we can solve the equation to obtain the reflection and transmission coefficients of all generated frequency harmonics for a monochromatic excitation of ω_k incident as:

$$R_\phi(\omega_k + n\omega_m) = e^{in\phi}R_0(\omega_k + n\omega_m) \quad (16)$$

$$T_\phi(\omega_k + n\omega_m) = e^{in\phi}T_0(\omega_k + n\omega_m) \quad (17)$$

where $R_0(\omega_k + n\omega_m) = B_1(\omega_k + n\omega_m)/A_1(\omega_k)$ and $T_0(\omega_k + n\omega_m) = A_2(\omega_k + n\omega_m)/A_1(\omega_k)$.